VARIATIONAL–BOUND NIP–ELEMENT METHOD APPLIED TO LONGITUDINAL LAMINAR FLOW IN ORDERED FIBROUS POROUS MEDIA

L. B. Machado[1], *E. A. Lisboa*[1] *and M. E. Cruz*[1]

[1] Mechanical Engineering Department, EE/COPPE/UFRJ, CP 68503, Rio de Janeiro, RJ, 21945–970, BRAZIL

Abstract

We apply a variational–bound nip–element method to calculate the longitudinal permeability for laminar flow in ordered fibrous porous media having arbitrary concentrations. Our hybrid analytico–computational approach handles the geometrically stiff problems associated with highly–packed media, by providing rigorous upper and lower bounds for the permeability. Our formulation is applicable to both ordered and random fibrous porous media; here we present and validate results for the permeability of the square and equilateral triangular arrays.

INTRODUCTION

Laminar flows in fibrous porous media are present in many natural and industrial phenomena. The complex microstructure of most fibrous porous media of interest precludes a complete local description of such flows. Engineering interest has thus focused on the determination of the macroscopic flow behavior, as characterized by effective properties (Jackson & James, 1986). Many different approaches have been adopted to calculate effective properties for flows in fibrous porous media: statistical microstructure–independent bound methods (Torquato, 1991), cell–model analytical (Happel, 1959) and semi–analytical treatments (Sparrow & Loeffler, 1959; Drummond & Tahir, 1984; Sangani & Yao, 1988), phenomenological modelling (Spielman & Goren, 1968; Ethier, 1991), and computational procedures (Edwards *et al.*, 1990; Cruz & Patera, 1995; Ghaddar, 1995). A systematic compilation of experimental measurements of effective properties for flows in fibrous porous media, to which calculated results may tentatively be compared to, is presented by Jackson & James (1986).

Two important classes of flows in fibrous porous media are the transverse and longitudinal (or parallel) laminar flows in systems composed of fixed monodisperse solid unidirectional circular cylinders distributed in the continuous incompressible Newtonian fluid phase (Jackson & James, 1986). Both flows are two–dimensional, the former having two velocity components, and the latter having one velocity component. The effective properties of interest are the Darcy transverse and longitudinal permeabilities. The positions of the cylinders, or fibers, may be orderly or randomly distributed in space. Longitudinal and transverse permeabilities are necessary for models which combine such results to predict the permeability of more complex three–dimensional arrangements (Jackson & James, 1986), and for many other applications (Drummond & Tahir, 1984). Ghaddar (1995) has recently studied the transverse flow case.

For the longitudinal permeability of unidirectional fibrous porous media, rigorous results for which precise error bounds are known, are still needed in the practically–relevant range of concentration values (or fiber volume fractions, c) corresponding to highly–packed media. Sparrow & Loeffler (1959) used truncated trigonometric series to approximately calculate the longitudinal permeability for the square and the equilateral triangle (or hexagonal) arrays, for a wide range of concentration values. However, slow convergence was observed for the square array as maximum packing ($c_{\max} = \pi/4$) was approached, and thus permeability values only up to $c = 0.72$ were given. Drummond & Tahir (1984) adapted the method of singularities to biharmonic equations, to derive expressions for the longitudinal (and transverse) permeabilities of several different ordered arrangements of cylinders, for the entire ranges of concentration values; however, they qualified their expressions as being reasonably accurate, and provided no error bounds for their high–c results. Sangani & Yao (1988) used a series expansion technique, restricted to linear problems, to compute the longitudinal (and transverse) permeability for both ordered and random fiber arrays; however, they did not compute permeability values for the range of concentrations corresponding to highly–packed fibers.

Although better suited than semi–analytical techniques to treat complex geometries and nonlinear phenomena, finite–element based computational procedures (Edwards *et al.*, 1990; Cruz & Patera, 1995) suffer from the severe geometric stiffness which arises when treating the distorted domains associated with highly–packed fibers. The boundaries of very close fibers form nip regions, or nips, that may be hard, or even impossible, to mesh, rendering numerical solutions either prohibitively expensive, due to excessive degrees–of–freedom and ill–conditioning, or hopeless. Cruz *et al.* (1995) and Ghaddar (1995) developed a variational–bound nip–element methodology to mitigate the problems caused by geometric stiffness, in the context of heat conduction in composites and transverse flow in fibrous porous media. The hybrid analytico–computational methodology is rigorously applicable to problems for which the effective property of interest is the extremum of a quadratic, symmetric,

positive–definite functional. The approach proceeds by an inner–outer decomposition of the geometrically stiff problem, in which analytical approximations in inner nip regions are folded into a modified outer problem defined over a geometrically more homogeneous domain. As a result, by virtue of the variational nature of the problem, rigorous upper and lower bounds for the effective property may be designed.

In this paper, we apply the variational–bound nip–element method to solve the problem of longitudinal laminar flow in unidirectional fibrous porous media having arbitrary concentration values, including maximum packing. (By arbitrary concentration we mean any possible concentration within the allowable range of concentrations for the given array of non–overlapping cylinders.) Our continuous and numerical formulations of the flow problem are applicable to both ordered and random fibrous porous media; however, in this paper we only compute the longitudinal permeability of the former. The porous medium is periodic, and we consider two types of periodic cells: the square array, composed of a circular fiber placed at the center of a square, and the equilateral triangular array, composed of a circular fiber placed at the center of a regular hexagon. The fiber–to–cell area ratio defines the concentration of the medium. Our computational procedure is validated by comparing longitudinal permeability results for the entire ranges of concentration values against previously obtained semi–analytical results. Furthermore, for each array, we present precise error bounds for the longitudinal permeability at maximum packing. Future work shall extend the current implementation to study longitudinal laminar flow in random fibrous porous media; such study is more relevant to practical applications, and it necessitates the variational–bound nip–element treatment developed here.

The paper is organized as follows. In the next section, we present the continuous formulation of the longitudinal laminar flow problem in the representative periodic cell of the fibrous porous medium. Next, we present and prove the microscale variational bounds for the longitudinal permeability. Subsequently, the numerical methods (mesh generation, finite–element discretization, and iterative solution) used for solving the problem are briefly described. Finally, in the last section, we present and validate our results, and state some concluding remarks.

LONGITUDINAL LAMINAR FLOW IN FIBROUS POROUS MEDIA

We consider here the longitudinal laminar flow in a unidirectional periodic fibrous porous medium, Ω, composed of monodisperse solid circular cylindrical fibers distributed in a fluid continuum. The fluid is assumed Newtonian, with constant density, ρ, and viscosity, μ. We further assume that the flow is hydrodynamically fully developed, thus inertia–free. By external means, a longitudinal pressure gradient of magnitude $\Delta P/L$ is imposed over the large scale L of Ω; L is the *macroscale*. The smallest scale of Ω is the diameter of the dispersed fibers, d, called the *microscale*. The *mesoscale* λ ($d \ll \lambda \ll L$) is the characteristic size of the periodic cell of area λ^2 containing N fibers; the concentration is thus given by $c = N\pi d^2/4\lambda^2$.

In Cruz and Patera (1995), a variational hierarchical scale–decoupling procedure is described, which decomposes the original multiscale problem in Ω into the microscale (length scale d), mesoscale (length scale λ), and macroscale (length scale L) problems. In the macroscale problem, not treated here, the longitudinal permeability, κ, is used in Darcy's law to calculate the bulk flow rate through the homogenized porous medium. In the mesoscale problem, the longitudinal permeability is actually computed by solving an appropriate periodic–cell problem. Finally, in the microscale problem, the nearfield behavior of clustered (nip–forming) fibers are modeled and subsequently incorporated into the mesoscale problem.

For the purposes of this paper, we are interested in the microscale–prepared mesoscale ordered–cell problem: to wit, we want to determine the longitudinal permeability as a function of the concentration, $\kappa(c)$, $0 < c \leq c_{\max}$, for the square and hexagonal arrays, Figure 1. The periodically replicated cell contains one fiber, $N = 1$, and the cell *fluid* domain is denoted $\Omega_{pc} \subset I\!R^2$. The center of the fiber is the origin of the rectangular coordinate system employed; on the plane of the paper, y_1 and y_2 are, respectively, the horizontal and the vertical axes, and y_3 is the axis perpendicular to both y_1 and y_2. The permeability κ is defined as the product of the viscosity μ and the superficial average y_3–velocity normalized by the magnitude of the driving pressure gradient $\Delta P/L$ set in the y_3 direction. As the concentration approaches the maximum packing value ($c_{\max} = \pi/4$ for the square array, $c_{\max} = \pi\sqrt{3}/6$ for the hexagonal array), the fiber in the cell forms nips with the fibers of neighbouring cells, necessitating microscale preparation (see next section).

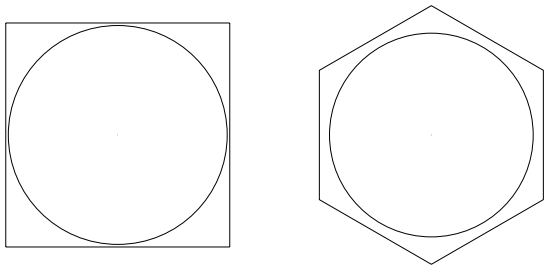

Figure 1: Geometries of the (a) square and (b) hexagonal cell domains, for the concentration $c = 0.75$.

In order to compute the longitudinal permeability

κ, we thus need to solve the longitudinal laminar fully–developed flow problem in Ω_{pc}, which is obtained from the original periodic multiscale problem in Ω by applying the method of homogenization (Bensoussan *et al.*, 1978; Mei & Auriault, 1989). Since the flow is laminar and fully–developed, the mass conservation equation is satisfied identically, the mesoscale velocity field has only one component, $\mathbf{u} = u_3(y_1, y_2)\mathbf{k}$ ($\mathbf{k}$ the unit vector in the y_3 direction), and the flow is inertia–free. The momentum equation thus reduces to the scalar Poisson equation (Sparrow & Loeffler, 1959; Sangani & Yao, 1988), with the viscous shearing stresses being balanced by the inhomogeneous pressure gradient term. Based on the analysis of Cruz & Patera (1995) for the mesoscale transverse flow problem, we deduce that the variational form associated with our (scalar Poisson) mesoscale longitudinal flow problem is given by

$$u_3 \;=\; \arg \max_{w_3 \in Y} J_{\Omega_{pc}}(w_3)\,, \tag{1}$$

where $J_{\mathcal{R}}$ is the functional defined by

$$J_{\mathcal{R}}(w_3) \;=\; \frac{2}{\mu}\frac{\Delta P}{L}\int_{\mathcal{R}} w_3\, d\mathbf{y} - \int_{\mathcal{R}} \frac{\partial w_3}{\partial y_j}\frac{\partial w_3}{\partial y_j}\, d\mathbf{y}\,. \tag{2}$$

In (1)–(2), summation over repeated indices is implied ($j = 1, 2$), $d\mathbf{y} = dy_1 dy_2$, Y is the function space $Y = \{w_3(y_1, y_2) \in H^1_{0\#}(\Omega_{pc})\}$, $H^1_{0\#}(\Omega_{pc})$ is the space of all λ–doubly periodic functions (subscript #) which vanish on $\partial\Omega_{pc,f}$, and for which both the function and derivative are square integrable over Ω_{pc}, and $\partial\Omega_{pc,f}$ is the surface of the fiber in the cell. In order to arrive at the standard velocity weak form, we take the first variation of the functional $J_{\Omega_{pc}}$, to obtain: Find $u_3(y_1, y_2) \in Y$ such that, $\forall v_3 \in Y$,

$$\mu \int_{\Omega_{pc}} \frac{\partial v_3}{\partial y_j}\frac{\partial u_3}{\partial y_j}\, d\mathbf{y} \;=\; \frac{\Delta P}{L}\int_{\Omega_{pc}} v_3\, d\mathbf{y}\,. \tag{3}$$

Once the mesoscale velocity field $u_3(y_1, y_2)$ has been found, the longitudinal permeability κ can be computed by evaluating the functional (Sangani & Yao, 1988)

$$\kappa \;=\; \frac{\mu}{\lambda^2}\frac{L}{\Delta P}\int_{\Omega_{pc}} u_3\, d\mathbf{y}\,, \tag{4}$$

which, in view of (3), can also be written as

$$\kappa \;=\; \frac{\mu^2}{\lambda^2}\frac{L^2}{\Delta P^2}\int_{\Omega_{pc}} \frac{\partial u_3}{\partial y_j}\frac{\partial u_3}{\partial y_j}\, d\mathbf{y}\,. \tag{5}$$

Clearly, the permeability κ is positive, and, because of (1) and (3), satisfies the following maximization principle, which is essential for constructing the microscale bounds presented in the next section:

$$\kappa \;=\; \frac{\mu^2}{\lambda^2}\frac{L^2}{\Delta P^2}\, J_{\Omega_{pc}}(u_3) \;=\; \frac{\mu^2}{\lambda^2}\frac{L^2}{\Delta P^2}\max_{w_3 \in Y} J_{\Omega_{pc}}(w_3)\,. \tag{6}$$

MICROSCALE VARIATIONAL BOUNDS

In Cruz *et al.* (1995) and Ghaddar (1995), the microscale component of the macro–meso–microscale formulation of Cruz & Patera (1995) is described and discussed in detail. For our purposes here, we want to formulate cluster models to avoid the nip regions between close fibers when the concentration is so high as to preclude mesh generation. In this section we present such nip–region–based cluster models appropriate for longitudinal laminar flow in fibrous porous media; the models lead to lower and upper bounds for the longitudinal permeability κ. Similar to previous developments (Ghaddar, 1995), the bounds rely on the maximization property, (6), of κ. The weak forms of the microscale–prepared mesoscale problems associated with the lower and upper bounds are almost identical to (3): one only has to replace the original cell fluid domain, Ω_{pc}, respectively, by the modified domains $\mathcal{C}_{LB}$ and $\mathcal{C}_{UB}$, defined below.

Nips Geometries

The geometries of the nip regions for the lower and upper bounds are shown in detail in Figure 2. As the concentration increases, the fiber in the cell gets very close to the fibers in the neighbouring cells; we postulate that a pair of close fibers forms a nip when the center–to–center separation distance $d + \alpha$ is less than $d + \alpha_c$, where α_c is a (small) prescribed parameter. For the lower bound, Figure 2(a), we define: $\mathcal{D}_{LB,n}$ is the domain of the lower bound nip region n, $n = 1, \ldots, N_n$, N_n is the number of nips in the cell ($N_n = 2$ for the square cell, $N_n = 3$ for the hexagonal cell); β is half the distance between the edges of $\mathcal{D}_{LB,n}$ parallel to the line joining the fibers centers; and $\mathcal{C}_{LB} = \Omega_{pc} \setminus \cup_{n=1}^{N_n} \mathcal{D}_{LB,n}$ is the modified mesoscale fluid domain. For the upper bound, Figure 2(b), we define: $\mathcal{D}_{UB,n}$ is the domain of the upper bound nip region n; β is half the length of the edge of $\mathcal{D}_{UB,n}$ perpendicular to the line joining the fibers centers; and $\mathcal{C}_{UB} = \Omega_{pc} \setminus \cup_{n=1}^{N_n} \mathcal{D}_{UB,n}$ is the modified mesoscale fluid domain.

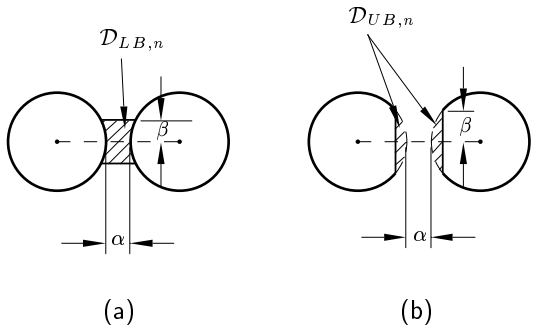

Figure 2: (a) Geometry of one lower–bound nip region, $\mathcal{D}_{LB,n}$. (b) Geometry of one upper–bound nip region, $\mathcal{D}_{UB,n}$.

In the next two subsections, we construct rigorous lower and upper bounds for the longitudinal permeability,

$$\kappa_{LB} \leq \kappa \leq \kappa_{UB} , \tag{7}$$

based only on solutions defined over $\mathcal{C}_{LB}$ and $\mathcal{C}_{UB}$, respectively: we avoid the impossible–to–mesh nip regions, while maintaining strict control over the resulting error.

Lower Bound

A lower bound for κ, κ_{LB}, can be obtained by simply plugging the flow in the nip regions $\mathcal{D}_{LB,n}$, $n = 1, \ldots, N_n$, N_n, decreasing the total available area for the longitudinal flow. Therefore, the weak form of the microscale–prepared mesoscale problem for the lower bound is: Find $u_{3,LB}(y_1, y_2) \in H^1_{0\#}(\mathcal{C}_{LB})$ such that, $\forall v_3 \in H^1_{0\#}(\mathcal{C}_{LB})$,

$$\mu \int_{\mathcal{C}_{LB}} \frac{\partial v_3}{\partial y_j} \frac{\partial u_{3,LB}}{\partial y_j} \, d\mathbf{y} = \frac{\Delta P}{L} \int_{\mathcal{C}_{LB}} v_3 \, d\mathbf{y} . \tag{8}$$

The expression for κ_{LB} is thus the functional

$$\kappa_{LB} = \frac{\mu}{\lambda^2} \frac{L}{\Delta P} \int_{\mathcal{C}_{LB}} u_{3,LB} \, d\mathbf{y} . \tag{9}$$

We now prove the bounding property of κ_{LB}.

We consider three flows, depicted in Figure 3 for one nip region. Flow (1) is the original flow in the fluid region Ω_{pc}, leading to the geometrically stiff problem whose solution is the velocity field $u_3 = u_3^{(1)}$ (which satisfies (3)). Flow (2) is the modified flow in the smaller fluid region $\mathcal{C}_{LB}$, leading to the nip–modified problem whose solution is the velocity field $u_{3,LB} = u_3^{(2)}$ given by (8). Flow (3) is the extension of flow (2) to the geometry of flow (1), such that the blockage regions $\mathcal{D}_{LB,n}$, $n = 1, \ldots, N_n$, are removed and replaced with fluid at rest; the stagnant flow in region n is denoted $\mathbf{0}_{\mathcal{D}_{LB,n}}$. The solution to flow (3) is the velocity field $u_3^{(3)}$. We want to show that the permeability κ_{LB} based on flow (2), given by (9), is a lower bound for the permeability κ based on flow (1), given by (4).

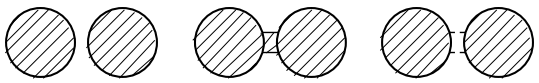

Flow (1) Flow (2) Flow (3)

Figure 3: Flows for the lower–bound proof.

In fact, we have, similarly to the presentation in Ghaddar (1995),

$$\begin{aligned} \kappa &= \frac{\mu^2}{\lambda^2} \frac{L^2}{\Delta P^2} J_{\Omega_{pc}}(u_3^{(1)}) \\ &\geq \frac{\mu^2}{\lambda^2} \frac{L^2}{\Delta P^2} J_{\Omega_{pc}}(u_3^{(3)}) \qquad (10) \\ &= \frac{\mu^2}{\lambda^2} \frac{L^2}{\Delta P^2} \left[J_{\mathcal{C}_{LB}}(u_3^{(2)}) + \cup_{n=1}^{N_n} J_{\mathcal{D}_{LB,n}}(\mathbf{0}_{\mathcal{D}_{LB,n}}) \right] \\ &= \frac{\mu^2}{\lambda^2} \frac{L^2}{\Delta P^2} J_{\mathcal{C}_{LB}}(u_3^{(2)}) = \kappa_{LB} . \qquad (11) \end{aligned}$$

The inequality (10) follows from (6) and the fact that the velocity field of flow (3) is an admissible candidate to the variational statement (1) defined over Ω_{pc}, since $u_3^{(3)} \in Y$. Flow (2) and flow (3) yield the same value for the functionals $J_{\mathcal{C}_{LB}}(u_3^{(2)})$ and $J_{\Omega_{pc}}(u_3^{(3)})$, respectively, because the quiescent fluid that replaces the nip regions in flow (3) does not contribute to the integrals in (2). Similarly to the proof above, it can further be shown that by decreasing β for a given geometry and/or concentration, the lower bound becomes sharper.

Upper Bound

An upper bound for κ, κ_{UB}, can be obtained by simply cutting each pair of close fibers as shown in Figure 2, yielding the regions $\mathcal{D}_{UB,n}$, $n = 1, \ldots, N_n$, which increase the total available area for the longitudinal flow. Therefore, the weak form of the microscale–prepared mesoscale problem for the upper bound is: Find $u_{3,UB}(y_1, y_2) \in H^1_{0\#}(\mathcal{C}_{UB})$ such that, $\forall v_3 \in H^1_{0\#}(\mathcal{C}_{UB})$,

$$\mu \int_{\mathcal{C}_{UB}} \frac{\partial v_3}{\partial y_j} \frac{\partial u_{3,UB}}{\partial y_j} \, d\mathbf{y} = \frac{\Delta P}{L} \int_{\mathcal{C}_{UB}} v_3 \, d\mathbf{y} ; \tag{12}$$

clearly, from the analysis of the previous section, $u_{3,UB}$ maximizes $J_{\mathcal{C}_{UB}}(w_3)$ over all functions $w_3 \in H^1_{0\#}(\mathcal{C}_{UB})$. The expression for κ_{UB} is thus the functional

$$\begin{aligned} \kappa_{UB} &= \frac{\mu}{\lambda^2} \frac{L}{\Delta P} \int_{\mathcal{C}_{UB}} u_{3,UB} \, d\mathbf{y} \qquad (13) \\ &= \frac{\mu^2}{\lambda^2} \frac{L^2}{\Delta P^2} \max_{w_3 \in H^1_{0\#}(\mathcal{C}_{UB})} J_{\mathcal{C}_{UB}}(w_3) . \qquad (14) \end{aligned}$$

We now prove the bounding property of κ_{UB}.

We again consider three flows, depicted in Figure 4 for one nip region. Flow (1) is the original flow in the fluid region Ω_{pc}, leading to the geometrically stiff problem whose solution is the velocity field $u_3 = u_3^{(1)}$ (which satisfies (3)). Flow (2) is the modified flow in the larger fluid region $\mathcal{C}_{UB}$, leading to the nip–modified problem whose solution is the velocity field $u_{3,UB} = u_3^{(2)}$ given by (12). Flow (3) is the extension of flow (1) to the geometry of flow (2), such that the cut regions $\mathcal{D}_{UB,n}$, $n = 1, \ldots, N_n$, are filled with fluid at rest; the stagnant flow in region n is denoted $\mathbf{0}_{\mathcal{D}_{UB,n}}$. The solution to flow (3) is the velocity field $u_3^{(3)}$. We want to show that the permeability κ_{UB} based on flow (2), given by (13), is an upper bound for the permeability κ based on flow (1), given by (4).

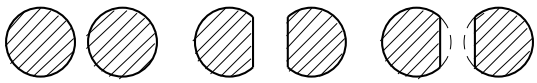

Figure 4: Flows for the upper–bound proof.

In fact, we have, similarly to the presentation in Ghaddar (1995),

$$\begin{aligned}
\kappa &= \frac{\mu^2}{\lambda^2}\frac{L^2}{\Delta P^2}\, J_{\Omega_{pc}}(u_3^{(1)}) \\
&= \frac{\mu^2}{\lambda^2}\frac{L^2}{\Delta P^2}\, [J_{\Omega_{pc}}(u_3^{(1)}) + \cup_{n=1}^{N_n} J_{\mathcal{D}_{UB,n}}(\mathbf{0}_{\mathcal{D}_{UB,n}})] \\
&= \frac{\mu^2}{\lambda^2}\frac{L^2}{\Delta P^2}\, J_{\mathcal{C}_{UB}}(u_3^{(3)}) \\
&\leq \frac{\mu^2}{\lambda^2}\frac{L^2}{\Delta P^2}\, J_{\mathcal{C}_{UB}}(u_3^{(2)}) \;=\; \kappa_{UB}\;. \qquad (15)
\end{aligned}$$

Flow (1) and flow (3) yield the same value for the functionals $J_{\Omega_{pc}}(u_3^{(1)})$ and $J_{\mathcal{C}_{UB}}(u_3^{(3)})$, respectively, because the quiescent fluid that fills the nip regions in flow (3) does not contribute to the integrals in (2). The inequality (15) follows from the maximization property (14) and the fact that the velocity field of flow (3) is an admissible candidate to the weak statement (12) defined over $\mathcal{C}_{UB}$, since $u_3^{(3)} \in H^1_{0\#}(\mathcal{C}_{UB})$. Again, similarly to the proof above, it can further be shown that by decreasing β for a given geometry and/or concentration, the upper bound becomes sharper.

NUMERICAL METHODS

Domain and Mesh Generation

The geometry generation procedure for the domains of our problem is fairly simple, and it simply consists of generating a circular cylinder inside a regular polygon (a square or a hexagon, Figure 1). For the finite–element corner–node distribution on the boundaries of the polygon and cylinder, we use the same boundary–node distribution function of Cruz & Patera (1995), given by

$$h_r^*(\mathbf{y}_b) \;\equiv\; \frac{h_r(\mathbf{y}_b)}{d} \;=\; \frac{1}{r}\left[\frac{(1/d)}{2/d_H(\mathbf{y}_b) + 1/h_0}\right]\;, \qquad (16)$$

where $\mathbf{y}_b$ denotes a boundary corner–node on either the polygon or the cylinder surface; h_r is the actual mesh spacing between two boundary corner–nodes; $d_H(\mathbf{y}_b)$ is the distance between the corner–node $\mathbf{y}_b$ on *one* boundary (either the polygon or the cylinder surface) and the closest point on the *other* boundary; h_0 is the input default mesh spacing; and r is the global mesh refinement parameter. As discussed in Cruz & Patera (1995), equation (16) possesses many desirable characteristics for our problem geometry; for example, by decreasing r, it is possible to uniformly refine the mesh (i.e., increase resolution) throughout the entire domain.

The positions of the corner–nodes on the boundaries, distributed according to equation (16), are then input to the mesh generation algorithm for the interior of the fluid region, Ω_{pc} for the original mesoscale problem, and, respectively, $\mathcal{C}_{LB}$ and $\mathcal{C}_{UB}$ for the lower–bound and upper–bound microscale–prepared mesoscale problems. We use a FORTRAN 77 implementation of a Delaunay triangulation algorithm, MSHPTG (Hecht & Saltel, 1990), to perform the triangular mesh generation for the appropriate fluid domain.

Figure 5 shows a typical mesh in Ω_{pc} for the original mesoscale problem in a square cell, for the concentration $c = 0.50$. Figures 6 and 7 show illustrative meshes in $\mathcal{C}_{LB}$ and $\mathcal{C}_{UB}$, respectively, for the lower–bound and upper–bound microscale–prepared mesoscale problems in a square cell, for the concentration $c = 0.785$. Figures 8 and 9 show illustrative meshes in $\mathcal{C}_{LB}$ and $\mathcal{C}_{UB}$, respectively, for the lower–bound and upper–bound microscale–prepared mesoscale problems in a hexagonal cell, for the concentration $c = 0.905$. We remark that for $c = 0.785$ in a square cell and for $c = 0.905$ in a hexagonal cell, it is not possible to generate meshes in Ω_{pc} using (16); the variational–bound nip–element treatment developed in this paper is therefore necessary for rigorous finite–element solution of the longitudinal flow problem in these higher concentrations.

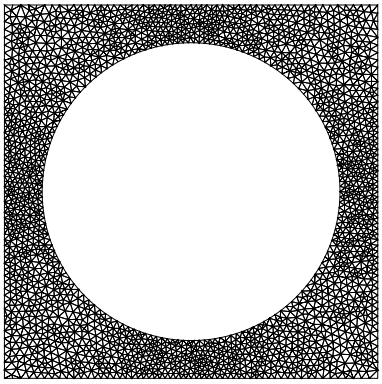

Figure 5: Finite–element mesh in Ω_{pc} for the square cell, $c = 0.50$: $h_0/d = 0.08$, $r = 2$, total of 4386 triangles and 2386 global corner–nodes.

Discretization and Solution

Finite element discretization is effected on the non–dimensional versions of the weak forms (3), (8) and (12). The discretization procedure consists of, first,

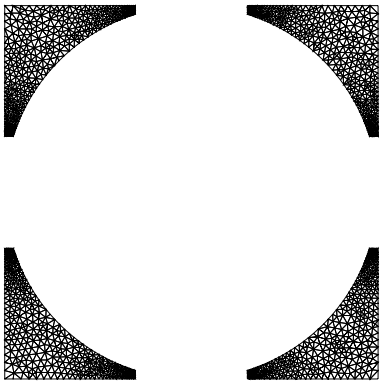

Figure 6: Finite–element mesh in $\mathcal{C}_{LB}$ for the square cell, $c = 0.785$: $\beta/d = 0.15$, $h_0/d = 0.08$, $r = 2$, total of 3122 triangles and 1791 global corner–nodes.

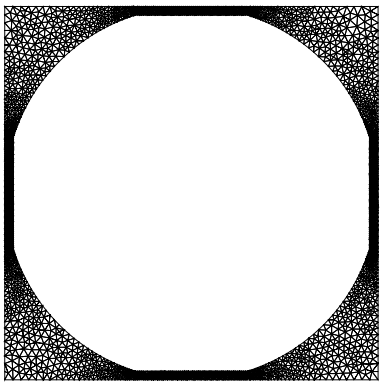

Figure 7: Finite–element mesh in $\mathcal{C}_{UB}$ for the square cell, $c = 0.785$: $\beta/d = 0.15$, $h_0/d = 0.08$, $r = 2$, total of 5610 triangles and 3235 global corner–nodes.

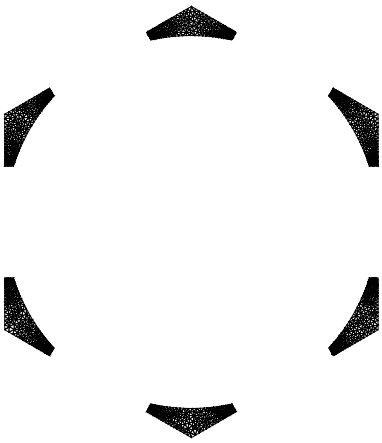

Figure 8: Finite–element mesh in $\mathcal{C}_{LB}$ for the hexagonal cell, $c = 0.905$: $\beta/d = 0.15$, $h_0/d = 0.08$, $r = 2$, total of 2568 triangles and 1509 global corner–nodes.

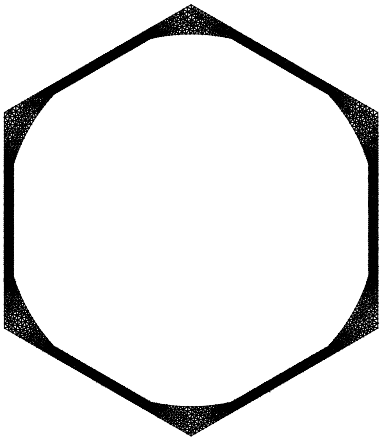

Figure 9: Finite–element mesh in $\mathcal{C}_{UB}$ for the hexagonal cell, $c = 0.905$: $\beta/d = 0.15$, $h_0/d = 0.08$, $r = 2$, total of 6162 triangles and 3603 global corner–nodes.

restricting the spaces of admissible functions to the finite element spaces, and, next, representing the finite element spaces with appropriate basis functions to generate a linear algebraic system of equations. In what follows we describe the discretization procedure for the original mesoscale problem in Ω_{pc}. The procedure for the lower–bound and upper–bound microscale–prepared mesoscale problems is similar: one only has to replace Ω_{pc} with $\mathcal{C}_{LB}$ and $\mathcal{C}_{UB}$, respectively.

The field variable of interest in the periodic cell is the longitudinal velocity u_3, $u_3 \in Y = H^1_{0\#}(\Omega_{pc})$, given by equation (3), rewritten here in the non–dimensional form

$$a(u_3^*, v_3) \;=\; l(v_3) \quad \forall v_3 \in Y \,, \tag{17}$$

where $u_3^* \equiv u_3/[(\Delta P/L)(d^2/\mu)]$, $a(w_3, v_3) = \int_{\Omega_{pc}} (\partial w_3/\partial y_j^*)(\partial v_3/\partial y_j^*) d\mathbf{y}^*$ is the bilinear form, $y^* \equiv y/d$, and $l(v)$ is the (non–dimensionalized) linear functional on the right–hand side of (3). The Galerkin approximation (Strang & Fix, 1973) to (17) is given by

$$a(u_{h,3}^*, v_3) \;=\; l(v_3) \quad \forall v_3 \in Y_h(\Omega_{pc,h}) \,, \tag{18}$$

where $u_{h,3}^*$ is the discrete approximation to u_3^*, $Y_h(\Omega_{pc,h}) = \{w_3|_{t_k} \in \mathcal{P}_1(t_k)\} \cap H^1_{0\#}(\Omega_{pc,h})$, $\mathcal{P}_1(t_k)$ is the space of all polynomials of degree 1 defined on the kth finite element (here a triangle) t_k, and the numerical domain $\Omega_{pc,h}$ is the linear "skin" of Ω_{pc}.

Finite element discretization concludes by expressing the basis and test functions in terms of the usual nodal Lagrangian interpolants, and performing all quadratures exactly, to arrive at the system

$$\underline{A}\,\underline{u}_{h,3}^* \;=\; \underline{F} \,, \tag{19}$$

where $\underline{A}$ is the global system matrix corresponding to the discrete (negative) Laplacian operator, $\underline{u}_{h,3}^*$ is the vector of unknown global nodal values of the scalar velocity field $u_{h,3}^*$, and $\underline{F}$ is the vector of global nodal val-

ues of the inhomogeneity $l(v_3)$. The Dirichlet boundary condition on $\partial\Omega_{pc,f}$ is incorporated into the matrix operator.

The discrete equation for κ_h^*, the numerical approximation to κ normalized by the square of the fiber diameter, is obtained by substituting $u_{h,3}$ for u_3 in equation (4),

$$\kappa_h^* = \frac{1}{d^2}\frac{\mu}{\lambda^2}\frac{L}{\Delta P}\int_{\Omega_{pc,h}} u_{h,3}\, d\mathbf{y} = \frac{1}{\lambda^{*2}}\int_{\Omega_{pc,h}} u_{h,3}^*\, d\mathbf{y}^*\,, \tag{20}$$

where $\lambda^* \equiv \lambda/d$. Alternatively, in view of (5), κ_h^* can also be written as

$$\kappa_h^* = \frac{1}{\lambda^{*2}}\, a(u_{h,3}^*\,, u_{h,3}^*)\,; \tag{21}$$

we calculate κ_h^* using both (20) and (21) as a way to verify the code.

Finally, we choose the well–known conjugate gradient algorithm (Golub & Van Loan, 1989), with no preconditioning, for iterative solution of the discrete problem (19). As usual, the iteration proceeds until a criterion for the incomplete–iteration error, based on the square of the norm of the residual, is satisfied. We have conducted several numerical tests, for both the square and hexagonal arrays, to choose the values for the incomplete–iteration error tolerance ϵ, the default mesh spacing $h_0^* \equiv h_0/d$, and the refinement parameter r. The chosen values are $h_0^* = 0.08$, $r = 3$ and $\epsilon = 10^{-6}$ for the square array, and $h_0^* = 0.08$, $r = 5$ and $\epsilon = 10^{-6}$ for the hexagonal array; these values ensure that the combined relative error in the permeability due to discretization and incomplete–iteration is at most 0.1% for both arrays.

RESULTS AND CONCLUSIONS

In this section we present our numerical results for the non–dimensional longitudinal permeability, $\kappa_h^* \equiv \kappa_h/d^2$, for both the square and hexagonal periodic arrays of fibers. The results have been grouped in three sets. The first set (Tables 1 and 2) contains values of κ_h^* for several concentrations for which it *is* possible to generate a mesh in Ω_{pc} using (16). The second set (Tables 3 and 4) contains values of the lower and upper bounds for κ_h^*, respectively $\kappa_{h,LB}^*$ and $\kappa_{h,UB}^*$, and of the permeability estimate $\overline{\kappa}_h^*$ and associated relative error $\overline{E}_r$, given by

$$\overline{\kappa}_h^* = \frac{1}{2}\,(\kappa_{h,LB}^* + \kappa_{h,UB}^*)\,, \tag{22}$$

$$\overline{E}_r = \frac{(\kappa_{h,UB}^* - \kappa_{h,LB}^*)/2}{\overline{\kappa}_h^*} \times 100\ \%\,, \tag{23}$$

for the two highest concentration values of the first set of results. The third set (Tables 5 and 6) contains values of $\kappa_{h,LB}^*$, $\kappa_{h,UB}^*$, $\overline{\kappa}_h^*$, and $\overline{E}_r$ for two concentration values, including maximum packing, for which it is *not* possible to generate a mesh in Ω_{pc} using (16).

Table 1: Longitudinal permeability results for the square array, for various values of the concentration c: our, κ_h^*, Sparrow & Loeffler's, κ_{SL}^*, and Sangani & Yao's, κ_{SY}^*, results. We write $1.0 \times 10^{-\mathrm{m}}$ as 1.0 E-m for m≥ 2.

c	κ_h^*	κ_{SL}^*	κ_{SY}^*
0.05	2.023	2.023	—
0.1	0.6382	0.6383	0.638
0.2	0.1603	0.1603	—
0.3	5.878 E-2	5.880 E-2	5.88 E-2
0.4	2.479 E-2	2.480 E-2	—
0.5	1.111 E-2	1.111 E-2	1.11 E-2
0.6	5.098 E-3	5.102 E-3	—
0.7	2.353 E-3	2.355 E-3	2.4 E-3
0.75	1.597 E-3	—	—
0.77	1.367 E-3	—	—

Tables 1 and 2 show values of κ_h^*, respectively, for the square and hexagonal arrays; also shown in the tables are the corresponding non–dimensional semi–analytical results of Sangani & Yao (1988), κ_{SY}^*, and calculated values of the approximate series solution of Sparrow & Loeffler (1959), κ_{SL}^*. It is clearly seen that our calculations agree with the previous results for all the tabulated values of the concentration. We observe that, for the same concentration, the hexagonal array has a lower permeability than the square array, which means that the former is more compact to the flow than the latter. We therefore expect, on physical grounds, that the hexagonal array will be more affected by the microscale treatment than the square array, for fixed $\alpha^* \equiv \alpha/d$ and $\beta^* \equiv \beta/d$.

Table 2: Longitudinal permeability results for the hexagonal array, for various values of the concentration c: our, κ_h^*, and Sparrow & Loeffler's, κ_{SL}^*, results. We write $1.0 \times 10^{-\mathrm{m}}$ as 1.0 E-m for m≥ 2.

c	κ_h^*	κ_{SL}^*
0.05	1.996	1.996
0.1	0.6250	0.6251
0.2	0.1537	0.1537
0.3	5.447 E-2	5.447 E-2
0.4	2.168 E-2	2.168 E-2
0.5	8.818 E-3	8.821 E-3
0.6	3.446 E-3	3.448 E-3
0.7	1.218 E-3	1.219 E-3
0.8	3.620 E-4	3.623 E-4
0.85	1.806 E-4	1.807 E-4
0.9	8.422 E-5	8.429 E-5

Tables 3 and 4 show values of $\kappa_{h,LB}^*$, $\kappa_{h,UB}^*$, $\overline{\kappa}_h^*$, and $\overline{E}_r$, respectively, for the square and hexagonal arrays, for concentration values for which it is possi-

Table 3: Longitudinal permeability bound results for the square array; $\beta^* \in \{0.23, 0.19, 0.16\}$, $c \in \{0.75, 0.77\}$ and $\alpha_c^* = 0.024$. We write $1.0 \times 10^{-\mathrm{m}}$ as 1.0 E-m.

c		$\beta^* = 0.23$	$\beta^* = 0.19$	$\beta^* = 0.16$
0.75	$\kappa_{h,LB}^*$	1.451 E-3	1.554 E-3	1.582 E-3
	$\kappa_{h,UB}^*$	1.787 E-3	1.652 E-3	1.616 E-3
	$\overline{\kappa}_h^*$	1.619 E-3	1.603 E-3	1.599 E-3
	$\overline{E}_r$	10.4%	3.1%	1.1%
0.77	$\kappa_{h,LB}^*$	1.267 E-3	1.343 E-3	1.360 E-3
	$\kappa_{h,UB}^*$	1.511 E-3	1.404 E-3	1.378 E-3
	$\overline{\kappa}_h^*$	1.389 E-3	1.374 E-3	1.369 E-3
	$\overline{E}_r$	8.8%	2.2%	0.66%

ble to generate a mesh in Ω_{pc} using (16). For the square array, $\beta^* \in \{0.23, 0.19, 0.16\}$, $c \in \{0.75, 0.77\}$ and $\alpha_c^* = 0.024$, and for the hexagonal array, $\beta^* \in \{0.23, 0.19, 0.15\}$, $c \in \{0.85, 0.90\}$ and $\alpha_c^* = 0.033$. The distance between a pair of neighbouring fibers, α^*, has to be smaller than the nip threshold parameter α_c^* for the pair to form a nip; thus, even though α^* is large enough to allow for mesh generation in Ω_{pc} for all those four concentrations, we use the artifact of setting α_c^* to a high value. We now make several remarks. First, consulting the respective lines in Tables 1 and 2, we note that the hierarchy of the bounds is obtained for all β^*: $\kappa_{h,LB}^* < \kappa_h^* < \kappa_{h,UB}^*$. Second, the gap $\Delta \equiv \kappa_{h,UB}^* - \kappa_{h,LB}^*$ gets progressively smaller (i.e., $\kappa_{h,LB}^*$ increases and $\kappa_{h,UB}^*$ decreases) as β^* decreases, and the average $\overline{\kappa}_h^*$ therefore approaches the numerical value κ_h^* obtained with no microscale treatment. Third, as expected, the relative errors corresponding to the bounds for the hexagonal array are worse than those for the square array (for comparison purposes, $\overline{E}_r$ for the hexagonal array corresponding to the values of α^* in Table 3 can be obtained, for example, by interpolating between the values in Table 4). Finally, the relative error

Table 4: Longitudinal permeability bound results for the hexagonal array; $\beta^* \in \{0.23, 0.19, 0.15\}$, $c \in \{0.85, 0.90\}$ and $\alpha_c^* = 0.033$. We write $1.0 \times 10^{-\mathrm{m}}$ as 1.0 E-m.

c		$\beta^* = 0.23$	$\beta^* = 0.19$	$\beta^* = 0.15$
0.85	$\kappa_{h,LB}^*$	3.408 E-5	1.081 E-4	1.549 E-4
	$\kappa_{h,UB}^*$	5.329 E-4	2.951 E-4	2.124 E-4
	$\overline{\kappa}_h^*$	2.835 E-4	2.016 E-4	1.837 E-4
	$\overline{E}_r$	88.0%	46.4%	15.7%
0.90	$\kappa_{h,LB}^*$	2.039 E-5	6.210 E-5	8.015 E-5
	$\kappa_{h,UB}^*$	2.810 E-4	1.345 E-4	9.380 E-5
	$\overline{\kappa}_h^*$	1.507 E-4	9.830 E-5	8.698 E-5
	$\overline{E}_r$	86.5%	36.8%	7.8%

decreases as the concentration increases, because the quotient of the area of $\mathcal{C}_{LB}$ (respectively, $\mathcal{C}_{UB}$) and the area of Ω_{pc} (the original flow area, equal to $(1-c)\lambda^2$) increases (respectively, decreases) as the concentration increases, for both arrays.

Table 5: Longitudinal permeability bound results for the square array; $\beta^* \in \{0.23, 0.19, 0.16\}$, $c \in \{0.785, \pi/4\}$ and $\alpha_c^* = 0.024$. We write $1.0 \times 10^{-\mathrm{m}}$ as 1.0 E-m.

c		$\beta^* = 0.23$	$\beta^* = 0.19$	$\beta^* = 0.16$
0.785	$\kappa_{h,LB}^*$	1.142 E-3	1.201 E-3	1.212 E-3
	$\kappa_{h,UB}^*$	1.330 E-3	1.242 E-3	1.223 E-3
	$\overline{\kappa}_h^*$	1.236 E-3	1.222 E-3	1.218 E-3
	$\overline{E}_r$	7.6%	1.7%	0.45%
$\pi/4$	$\kappa_{h,LB}^*$	1.139 E-3	1.197 E-3	1.208 E-3
	$\kappa_{h,UB}^*$	1.326 E-3	1.238 E-3	1.219 E-3
	$\overline{\kappa}_h^*$	1.233 E-3	1.218 E-3	1.214 E-3
	$\overline{E}_r$	7.6%	1.7%	0.45%

Table 6: Longitudinal permeability bound results for the hexagonal array; $\beta^* \in \{0.15, 0.12\}$, $c \in \{0.905, \pi\sqrt{3}/6\}$ and $\alpha_c^* = 0.002$. We write $1.0 \times 10^{-\mathrm{m}}$ as 1.0 E-m.

c		$\beta^* = 0.15$	$\beta^* = 0.12$
0.905	$\kappa_{h,LB}^*$	7.449 E-5	7.716 E-5
	$\kappa_{h,UB}^*$	8.590 E-5	7.941 E-5
	$\overline{\kappa}_h^*$	8.020 E-5	7.829 E-5
	$\overline{E}_r$	7.1%	1.4%
$\frac{\pi\sqrt{3}}{6}$	$\kappa_{h,LB}^*$	7.241 E-5	7.489 E-5
	$\kappa_{h,UB}^*$	8.306 E-5	7.690 E-5
	$\overline{\kappa}_h^*$	7.774 E-5	7.590 E-5
	$\overline{E}_r$	6.8%	1.3%

Tables 5 and 6 show values of $\kappa_{h,LB}^*$, $\kappa_{h,UB}^*$, $\overline{\kappa}_h^*$, and $\overline{E}_r$, respectively, for the square and hexagonal arrays, for concentration values for which it is not possible to generate a mesh in Ω_{pc} using (16). For the square array, $\beta^* \in \{0.23, 0.19, 0.16\}$, $c \in \{0.785, c_{\max} = \pi/4\}$, and $\alpha_c^* = 0.024$, and for the hexagonal array, $\beta^* \in \{0.15, 0.12\}$, $c \in \{0.905, c_{\max} = \pi\sqrt{3}/6\}$, and $\alpha_c^* = 0.002$. Sparrow & Loeffler (1959) calculate the longitudinal permeability at maximum packing *only* for the hexagonal array; their result is $\kappa_{SL}^*(c_{\max} = \pi\sqrt{3}/6) = 7.543 \times 10^{-5}$. We achieve the small relative errors of 0.45% and 1.3% at maximum packing for the square and hexagonal arrays, respectively. Of course, the relative errors due to the bounds, $\overline{E}_r$, have to be combined with the relative error of 0.1% due to numerical solution, yielding a total (added) relative error of 0.55% and 1.4% in the values of $\overline{\kappa}_h^*$ for the square and hexagonal arrays, respectively.

We conclude that we have successfully extended the variational–bound nip–element methodology of Cruz *et al.* (1995) and Ghaddar (1995) to study longitudinal laminar flow in ordered fibrous porous media. We have provided precise error bounds for the longitu-

dinal permeability at maximum packing for both the square and hexagonal arrays. Future work shall extend the current implementation to calculate the longitudinal permeability of two–dimensional *random* arrays of fibers, which are more relevant to the study of real systems and processes (Jackson & James, 1989; Ethier, 1991).

ACKNOWLEDGEMENTS

M. E. C. and L. B. M. would like to gratefully acknowledge the support of the Brazilian Council for Development of Science and Technology (CNPq) through Grant 521002/97–4, FAPERJ through Grant E–26/150.654/97, and CAPES. We all thank the Laboratory of Transmission and Technology of Heat of EE/COPPE/UFRJ and the NACAD/COPPE/UFRJ for providing us with the necessary computational resources for our calculations. We finally thank Mr. Alan D. C. Marques for his help with some figures.

REFERENCES

Bensoussan, A., Lions, J.–L. & Papanicolaou, G. C., 1978, *Asymptotic Analysis for Periodic Structures*, North–Holland Publishing Co., Amsterdam.

Cruz, M. E. & Patera, A. T., 1995, A Parallel Monte–Carlo Finite–Element Procedure for the Analysis of Multicomponent Random Media, *Int. J. Numer. Methods Engng.*, vol. 38, pp. 1087–1121.

Cruz, M. E., Ghaddar, C. K. & Patera, A. T., 1995, A variational–bound nip–element method for geometrically stiff problems; application to thermal composites and porous media, *Proc. R. Soc. Lond.* A, vol. 449, pp. 93–122.

Drummond, J. E. & Tahir, M. I., 1984, Laminar Viscous Flow Through Regular Arrays of Parallel Solid Cylinders, *Int. J. Multiphase Flow*, vol. 10, pp. 515–540.

Edwards, D. A., Shapiro, M., Bar–Yoseph, P. & Shapira, M., 1990, The influence of Reynolds number upon the apparent permeability of spatially periodic arrays of cylinders, *Phys. Fluids* A, vol. 2, pp. 45–55.

Ethier, C. R., 1991, Flow Through Mixed Fibrous Porous Materials, *A.I.Ch.E. Journal*, vol. 37, pp. 1227–1236.

Ghaddar, C. K., 1995, On the permeability of unidirectional fibrous media: a parallel computational approach, *Phys. Fluids*, vol. 7, pp. 2563–2589.

Golub, G. H. & Van Loan, C. F., 1989, *Matrix Computations*, 2nd ed., The Johns Hopkins University Press, Baltimore, Maryland.

Happel, J., 1959, Viscous Flow Relative to Arrays of Cylinders, *A.I.Ch.E. Journal*, vol. 5, pp. 174–177.

Hecht, F. & Saltel, E., 1990, Emc2: Editeur de maillages et de contours bidimensionnels, Manuel d'utilisation, Rapport Technique No. 118, INRIA, France.

Jackson, G. W. & James, D. F., 1986, The Permeability of Fibrous Porous Media, *Can. J. Chem. Eng.*, vol. 64, pp. 364–374.

Mei, C. C. & Auriault, J.–L., 1989, Mechanics of heterogeneous porous media with several spatial scales, *Proc. R. Soc. Lond.* A, vol. 426, pp. 391–423.

Sangani, A. S. & Yao, C., 1988, Transport processes in random arrays of cylinders. II. Viscous flow, *Phys. Fluids*, vol. 31, pp. 2435–2444.

Sparrow, E. M. & Loeffler Jr., A. L., 1959, Longitudinal Laminar Flow Between Cylinders Arranged in Regular Array, *A.I.Ch.E. Journal*, vol. 5, pp. 325–330.

Spielman, L. & Goren, S. L., 1968, Model for Predicting Pressure Drop and Filtration Efficiency in Fibrous Media, *Env. Sci. Tech.*, vol. 2, pp. 279–287.

Strang, G. & Fix, G. J., 1973, *An Analysis of the Finite Element Method*, Prentice–Hall, Inc., Englewood Cliffs, NJ.

Torquato, S., 1991, Random heterogeneous media: Microstructure and improved bounds on effective properties, *Appl. Mech. Rev.*, vol. 44, pp. 37–76.